



HAL
open science

Equivalent electrical model for high current density zinc electrodeposition

Léo Fayard, Vincent Bizouard, Vincent Feynerol, Henri Schneider, Christophe Turpin

► **To cite this version:**

Léo Fayard, Vincent Bizouard, Vincent Feynerol, Henri Schneider, Christophe Turpin. Equivalent electrical model for high current density zinc electrodeposition: Investigation through polarization curves and electrochemical impedance spectroscopy. *International Journal of Electrochemical Science*, 2023, 18 (7), 10.1016/j.ijoes.2023.100185 . hal-04625668

HAL Id: hal-04625668

<https://hal.science/hal-04625668>

Submitted on 26 Jun 2024

HAL is a multi-disciplinary open access archive for the deposit and dissemination of scientific research documents, whether they are published or not. The documents may come from teaching and research institutions in France or abroad, or from public or private research centers.

L'archive ouverte pluridisciplinaire **HAL**, est destinée au dépôt et à la diffusion de documents scientifiques de niveau recherche, publiés ou non, émanant des établissements d'enseignement et de recherche français ou étrangers, des laboratoires publics ou privés.



Distributed under a Creative Commons Attribution - NonCommercial - NoDerivatives 4.0 International License



Equivalent electrical model for high current density zinc electrodeposition: Investigation through polarization curves and electrochemical impedance spectroscopy

Léo Fayard^{a,b,*}, Vincent Bizouard^a, Vincent Feynerol^a, Henri Schneider^b, Christophe Turpin^b

^a ERGOSUP, 145 chemin de la Roche du Guide, Malataverne 26780, France

^b Université de Toulouse, Laboratoire LAPLACE, UMR 5213 CNRS-INPT-UPS, 31071 Toulouse Cedex, France

ARTICLE INFO

Keywords:

Electrical Circuit Modelling
Zinc electrodeposition
Decoupled water electrolysis
Electrochemical Impedance Spectroscopy
Polarization curves

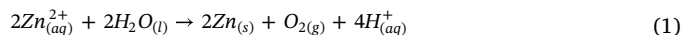
ABSTRACT

Polarization resistance of a batch process at 2000 Am⁻² of zinc electrodeposition is investigated by means of Electrochemical Impedance Spectroscopy (EIS) and polarization curves U(j). This work proposes EIS and U(j) characterisations over time with current density range from 50 Am⁻² to 4000 Am⁻², corresponding to a variation from [H₂SO₄] = 130 gL⁻¹ and [Zn²⁺] = 120 gL⁻¹ to approximately [H₂SO₄] = 280 gL⁻¹ and [Zn²⁺] = 20 gL⁻¹. A drift correction of EIS measurement using linear interpolation in time is provided. These measurements allow for the observation of the main physicochemical reactions occurring during the Ergosup batch process and contributing to the polarization resistance of zinc electrodeposition at high current density: charge transfer and adsorption at the cathode, charge transfer and mass transport at the anode. Simplified reaction mechanisms are used and has led to the development of an equivalent electrical model, which accounts for the various phenomena observed during the process. The equivalent electrical model is developed from the kinetic equations describing the electrochemical process. The model is able to reproduce the experimental impedance curves at high current densities with high correlation coefficients ($R^2 > 0.9990$).

1. Introduction

While the consumption of grey and black hydrogen from gas and coal is constantly increasing, green hydrogen from water electrolysis accounts for only 0.04% of the world's 94 Mt H₂ production in 2021 [1]. Thus, the production of hydrogen from electrolysis with low-carbon electricity remains an important decarbonisation tool for industries that require it, such as fertiliser or methanol production, or as a chemical reagent for desulphurisation. In this context, Ergosup offers an innovative process to produce hydrogen [2].

The process developed by Ergosup uses zinc as a vector in order to decouple the production of oxygen and hydrogen in two steps during the electrolysis of water. First, the zinc is electrodeposited, the oxygen is released and the electrolyte acidifies according to the equation:



In this step, the zinc reduction reaction competes with the proton reduction, producing hydrogen which is therefore lost. The proportion

of current going into the zinc reduction is characterized by the Faraday efficiency η_F .

The zinc is then dissolved in a second step and leads to the production of hydrogen, according to:



Thus, after the electrolysis phase (1) the Ergosup process cleverly uses the spontaneity of the second equation (2) to return to the original point and run a batch process. Indeed, the resultant of these two equations is equivalent to the electrolysis of water. It has the advantages of being able to decouple the consumption of electricity and the production of hydrogen over time, and to offer energy storage in metallic and ionic form. Finally, the separate production of hydrogen in step (2) allows the pressure to rise up to 350 bars through the accumulation effect in the container.

During operations, typical industrial concentrations of electrolyte for zinc production in acidic media are nearly constant and change by about 5 gL⁻¹. These concentrations range from 50 – 70 gL⁻¹ for zinc

* Corresponding author at: ERGOSUP, 145 chemin de la Roche du Guide, Malataverne 26780, France.

E-mail address: leo.fayard@laplace.univ-tlse.fr (L. Fayard).

Nomenclature*List of Symbols*

F	Faraday constant
$[X_i]$	Concentration of the electroactive species X_i
D	Diffusion coefficient
R	Universal gas constant
e	Thickness of the zinc layer
E	Electrode potential
S	Geometric area
T	Temperature
Z	Impedance
p	Laplace variable
$Re(Z)$	Real part of the number Z
$Im(Z)$	Imaginary part of the number Z
f	Frequency
Δj	Ac part of the current perturbation
ΔE	Ac part of the potential perturbation
R_{ct}	Charge transfer resistance
C_{dl}	Double-layer capacitance
R_{Ω}	Electrolyte resistance
R_{δ}	Diffusion impedance resistance
W_{δ}	Diffusive Warburg element
C_{θ}	Adsorbates impedance capacitance
R^2	Determination coefficient
R_{θ}	Adsorbates impedance resistance
L_{Ω}	Inductance induced
k	Kinetic constant of half reaction
K	Kinetic constant
n	Number of electrons involved in the electrochemical reaction

i	Current
j	Current density
j_0	Exchanged current density
J	Interfacial transport flow
s	Superficial site
w	Pulse

Greek

α	Charge transfert coefficient
δ	Nernst layer thickness
σ	Conductivity
σ_0	Conductivity in bubble free electrolyte
Γ	Total number of sites per unit area
θ_i	Coverage ratio of a species i
η_F	Faraday efficiency
τ_{δ}	Diffusion impedance time constant

Postscript

o	Oxidation
r	Reduction
ads	Adsorption
th	Theoretical
obj	Objective
nom	Nominal
EIS	Electrochemical Impedance Spectroscopy
Mod	Modelled
(g)	Gaseous
(aq)	Aqueous
(s)	Solid

and from 130 – 180 gL⁻¹ for sulphuric acid, depending on the plant [3,4]. Wider concentration ranges have been studied by authors, as 27 – 107 gL⁻¹ for zinc and 95 – 228 gL⁻¹ for acid [5]. The current density of the deposit is commonly in the range of 400 Am⁻² to 500 Am⁻². Various authors have already characterised the impedance and voltage-current density curves of zinc electrodeposition [6–9,10]. In order to explain the multiple stationary states and the release of hydrogen during the electrolysis of zinc, they proposed a mechanism for the electrocrystallisation of zinc including both the autocatalytic step $Zn^{2+} + Zn_{ads}^+ + e^- = 2Zn_{ads}^+$ and the presence of adsorbates of which H_{ads}^+ and Zn_{ads}^+ . Later, the model was completed with the presence of active reaction catalyst sites [11] and H_2 evolution on oxides ZnO or ZnOH at low current densities [8], however assumed to be zero at high current density given the strong polarization [12]. The reaction mechanism is still subject to discussion depending on the operating conditions, the kinetic parameters having a high variability and low reproducibility [13].

However, these characterisations have never been carried out under conditions similar to the Ergosup batch process, where zinc concentration variations of about 100 gL⁻¹ are realized in a couple of hours before being reversed. The evolution of the concentrations being necessary with the intention of increasing the compactness of the system in order to reduce the costs. Furthermore, the characterisation never takes into account the oxygen evolution which is studied separately.

This study proposes to characterise in situ the first step of the process during its execution in order to model it. This characterisation then makes it possible to establish a diagnosis of the energy consuming step according to the operating conditions (concentrations, temperature, current density). The overall modelling of the process, which draws parallels between physical-chemical and electrical phenomena, is

essential for incorporating the process into electrical system simulation tools. These tools, particularly developed in the Laplace laboratory, enable the examination of direct coupling between the electrolyzer and renewable energy sources, as well as the study of system ageing through characterizations performed throughout its lifecycle.

This study aims to provide such a modelling for the Ergosup batch process by characterising the evolution of polarization resistances, as well as other electrochemical parameters, during the process operating at high current densities. Polarization curves and impedance spectroscopy will be used, with a drift correction of the electrolytic resistance thanks to high frequency impedance measurements.

2. Experimental

2.1. Electrolysis cell

The anode is a 2 mm thick titanium plate covered with 2 μ m Mixed Metal Oxide (MMO, UMICORE), and the cathode is a 3 mm thick plate of zirconium (UMICORE). A pure electrolyte is prepared from ZnO powder (Fisher Chemical, purity $\geq 99.5\%$), H_2O and H_2SO_4 37.4 wt% (Lab-Online). Initial concentrations are $[H_2SO_4] = 130 \text{ gL}^{-1}$ and $[Zn^{2+}] = 120 \text{ gL}^{-1}$.

The electrodes are immersed in a double-wall 1 L beaker whose temperature is maintained at $40 \pm 2^\circ\text{C}$. They are kept parallel at a distance of 5 mm with 4 PTFE washers at the top of the assembly and a spacer at the bottom of the electrodes. The active geometric area of the electrodes is a rectangle of 100 cm² (7.00 \times 14.28 cm), delimited by Teflon tape. The volume of electrolyte is 333 mL, which is small compared to the size of the electrodes, in order to make the batch process evolve in a reasonable time. The remaining volume of the beaker is then occupied by a PVDF support. A stirring with a cylindrical magnetic bar of

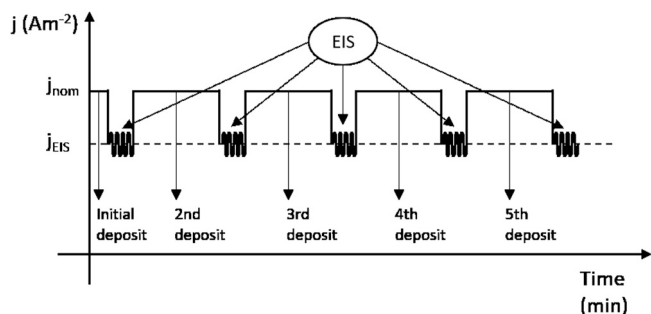


Fig. 1. Picture of the experimental setup.

15 mm with ring homogenizes the electrolyte before running the experimental procedure. Stirring continues during the experimental procedure in order to prevent diffusion limitations. The experimental setup is shown in Fig. 1.

2.2. Experimental procedure

2.2.1. Principle of batch characterisation

The current study focuses on the polarization resistance at five different times during the deposition step at nominal current density j_{nom} (Am^{-2}). The operating conditions evolve in the batch process, which is without any adjustment, so the polarization resistance varies over time. Each characterisation is separated by a deposit period, as an example is shown in Fig. 2 with impedance spectroscopy. Characterisation times are important for comparison with normal zinc electro-deposition, however the important point is the cumulative electrical charge.

The characterisation takes place at regular intervals over a period of 90 min at j_{nom} . The characterisation times are given as if a constant current of 2000 Am^{-2} had been applied up to the time of characterisation, and are shown in Table 1 with the related concentrations of the electrolyte. Given that electrical charge are different at each type of characterisation, the deposition times are adapted in order to have the desired electrical charge at characterisation times, that is to say in order to have iso-coulomb characterisations.

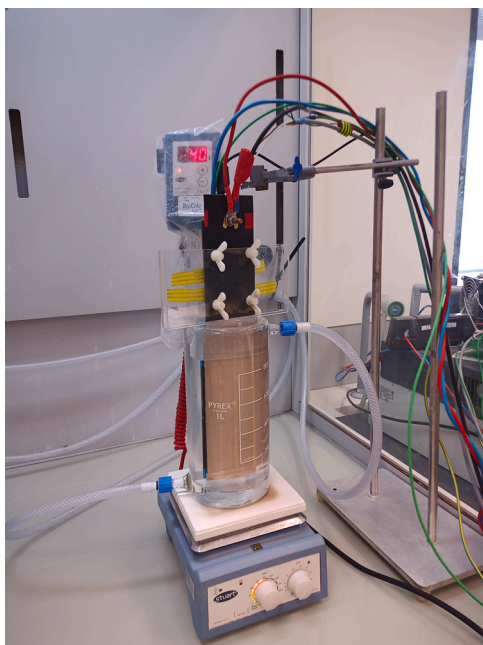


Fig. 2. Profile of the characterisation current over time. j_{nom} is the nominal current density of zinc deposition. j_{EIS} is the characterisation current density.

Table 1

Theoretical concentrations calculated with $\eta_F = 0.92$ at different characterisations times.

Time (min)	Charge (kC)	$[\text{Zn}^{2+}]$ (gL^{-1})	$[\text{HSO}_4^-]$ (gL^{-1})	$[\text{SO}_4^{2-}]$ (gL^{-1})	$[\text{H}^+]$ (gL^{-1})	pH
3	3.6	116.6	263.5	42.8	0.04	1.40
22.5	27	94.7	300.7	5.96	0.33	0.48
45	54	69.4	304.8	1.87	1.08	-0.03
67.5	81	44.1	305.6	1.09	1.86	-0.27
90	108	18.9	305.9	0.77	2.61	-0.42

At these 5 characterisation times, impedance spectroscopy measurements and polarization curves are made in identically replicated experiments.

2.2.2. Impedance studies

The system to analyse the impedance of the cell includes both the waveform generator and the impedance analyser. In order to characterise the cell at nominal point of operation, the impedance analyser must achieve high intensity (20 A) and high frequency (20 kHz). The waveform generator drives parallel active loads in series with a power supply that provides electricity to the electrolysis cell (refer to Supplementary Materials).

The galvano electrochemical measurement was conducted over the frequency range from 20 kHz to 50 mHz with DC part of the current filtered above 100Hz. The measurement frequencies were selected manually in order to limit their duration, especially at low frequencies. At the end of the impedance measurement, a second EIS takes place from 20 kHz to 1 kHz, as discussed later in part 2.3. The characterisation principle is used for current densities of characterisation j_{EIS} : 50 Am^{-2} , 100 Am^{-2} , 200 Am^{-2} , 500 Am^{-2} , 1000 Am^{-2} , 2000 Am^{-2} and 3000 Am^{-2} , with current variation of $\pm 10\%$. The quality of the measurement is guaranteed by monitoring the linearity of sinusoidal signals by measuring the total harmonic distortion (THD, refer to Supplementary materials).

2.2.3. Polarization curves

The same characterisation principle is applied to obtain the polarization curves during the process. The characterisation consists of 16 successive stages of increasing intensity j_{step} : 25 Am^{-2} , 50 Am^{-2} , 75 Am^{-2} , 100 Am^{-2} , 150 Am^{-2} , 200 Am^{-2} , 350 Am^{-2} , 500 Am^{-2} , 750 Am^{-2} , 1000 Am^{-2} , 1500 Am^{-2} , 2000 Am^{-2} , 2500 Am^{-2} , 3000 Am^{-2} , 3500 Am^{-2} and 4000 Am^{-2} . The choice was made to limit each step to the same charge of 150 C. This value is a compromise between the time needed to fill the electric double layer but also remaining in a quasi-stationary state, given that the Ergosup process is not stationary. The ohmic correction of the polarization curves is done through high frequency (20–1 kHz) measurement of the ohmic resistance, R_Ω being approximately determined experimentally as the projection of the highest frequency point on the x-axis on the Nyquist plane. Indeed, the signature of a pure resistance in the Nyquist plane is expressed by a simple shift of the real axis.

2.3. Impedance ohmic drop correction

As presented by Lasia in his book [14], in the case of non-stationary systems it is possible to proceed to a linear interpolation of the impedance as a function of frequency and time by recording a series of impedance measurement at distinct time intervals. As all parameters are likely to vary during the measurement, the main variation comes from the electrolytic resistance R_Ω due to the variation of $[\text{H}_2\text{SO}_4]$ and $[\text{Zn}^{2+}]$, as confirmed in the last part. Therefore, it is possible to proceed to a second EIS at high frequencies in order to evaluate the variation of R_Ω during the measurement. Then, it is possible to propose a linear time

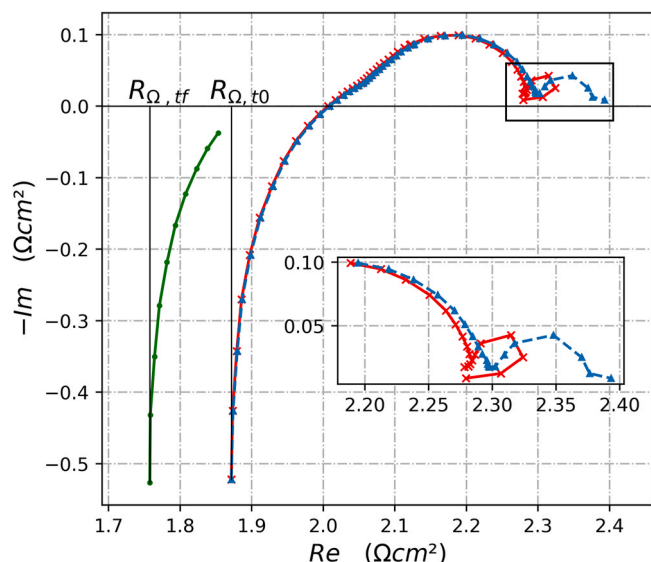


Fig. 3. Ohmic drop correction of the first EIS measured at $t = 3$ min (a) Uncorrected curve - red, (b) Specific high frequency EIS truncated at 4133 Hz - green and (c) Temporally corrected curve according to eq. (3) - blue.

correction of the impedance at each frequency or pulsation $\omega = 2 * \pi * f$ evaluation during the measurement:

$$Z_{cor}(\omega, t) = Z(\omega) + (R_{\Omega,t0} - R_{\Omega,tf}) \frac{t - t0}{\Delta t_{measure}} \quad (3)$$

Fig. 3 shows the first whole impedance measurement at nominal operating point $j = 2000 \text{ Am}^{-2}$. The high frequencies EIS (green) 20–1 kHz reproduces the spectrum of the uncorrected measure (red) with a shift to the left on the real axis, corresponding to the decrease of Pouillet's resistance with increasing acidity during the measurement (see section 3.1). During initial impedance measurement, the drift is particularly important at low frequencies due to the lengthening of the measurement time as the frequency decreases. The correction allows the reconstruction of impedance data at low frequencies at initial measurement time, as if the system were stable.

3. Theoretical

3.1. Electrolytic resistance

The ohmic drop in the electrodes is neglected compared to the one of the electrolyte. The ohmic resistance in the electrolyte is modelled by a modified Pouillet's law [15,16]:

$$R_{\Omega} = \frac{e}{\sigma * S} = \frac{e}{\sigma_0 * \frac{1-\alpha}{1+\frac{\alpha}{2}} * S} \quad (4)$$

e (m) represents the distance between the electrodes, S (m^2) is the active area and α (unitless) is the vacuum rate in the electrolyte. The conductivity σ (Sm^{-1}) is differentiated from the one of a continuous medium σ_0 . Indeed, the conductivity σ of the bulk electrolyte is dependent of the presence of dispersed gas bubble produced at the anode O_2 and at the cathode H_2 during step (1), as referenced [17,18]. The H_2 evolution reaction is likely to change over time, thus changing α during the process. σ_0 is a function of concentrations and temperature, and can therefore be measured or estimated empirically according to (corrected for $\text{Mg}^{2+} = \text{ions}$) [19]:

$$\sigma_0 = 0.4 + 0.115(T - 273) + 0.282[\text{H}_2\text{SO}_4](T - 273) + 34.42[\text{H}_2\text{SO}_4] - 4.51[\text{H}_2\text{SO}_4]^2 + 2.86[\text{Zn}^{2+}]^2 + [\text{Zn}^{2+}](-0.114(T - 273) - 10.58[\text{H}_2\text{SO}_4] - 2.24) \quad (5)$$

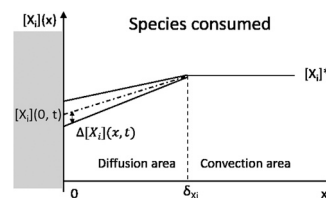


Fig. 4. Stationary profiles of species concentration and its perturbation as a function of distance x from the electrode surface.

This equation clearly demonstrates that during the electrodeposition step (1) the conductivity increases substantially, thus decreasing the electrical resistance of the electrolyte.

3.2. Mass transport

Mass transport in the case of stationary electrodes in a moving fluid is usually represented by the Nernst diffusion-convection theory. This assumes a length δ_{X_i} (m) of electrolyte where only diffusion ensures the transport of species X_i of concentration $[X_i]$ (molcm^{-3}). Beyond δ_{X_i} , the electrolyte is assumed to be perfectly stirred and the concentration is independent of the distance to the electrode—solution interface.

In the absence of convection, the mass transport is described by Fick's 2nd law:

$$\frac{\partial [X_i](x, t)}{\partial t} = D_{X_i} \frac{\partial^2 [X_i](x, t)}{\partial x^2} \quad (6)$$

Where D_{X_i} (m^2s^{-1}) is the diffusion coefficient of species X_i .

The integration in steady state with the condition $[X_i](\delta_{X_i}) = [X_i]^*$, where $[X_i]^*$ is the bulk concentration of X_i , gives the affine law of concentration of the species $[X_i]$ as a function of the distance x , as shown in **Fig. 4**:

$$[X_i](x) = [X_i](0) + \frac{[X_i]^* - [X_i](0)}{\delta_{X_i}} x \quad (7)$$

The Fick's 2nd law being linear in $[X_i]$, the concentration of the equation (6) can be replaced by its perturbation around its stationary value:

$$\frac{\partial \Delta [X_i](x, t)}{\partial t} = D_{X_i} \frac{\partial^2 \Delta [X_i](x, t)}{\partial x^2} \quad (8)$$

3.3. Electric double layer

The presence of an electric double layer is observed as a result of charge accumulation at the interface between the electrode and the electrolyte. It is assumed, for simplicity, that the current crossing the electrode-electrolyte interface is the sum of the Faradaic current and the capacitive current:

$$j(t) = j_f(t) + \frac{dC_{dl}E(t)}{dt} \quad (9)$$

Thus, the electrode impedance Z (Ωcm^2) is written as the parallelisation, shown in **Fig. 5**, of the double layer capacitance per unit area C_{dl} (Fcm^{-2}) to the Faradaic impedance:

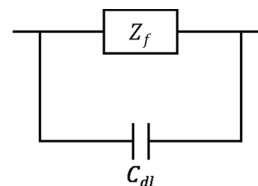


Fig. 5. Equivalent electrical circuit of an electrochemical reaction.

$$Z(p) = \frac{Z_f}{1 + pC_{dl}Z_f} \quad (10)$$

3.4. Faradaic impedance of a concentration-depleted redox reaction

In the case of an oxidation reaction of the type:



with interfacial depletion of reducing agent R and neglecting the reverse reaction due to the high polarization, the reaction rate is written:

$$v_o(t) = K_o(t)[R](0, t) \quad (12)$$

using the definition of the kinetic constant $K_o(t)$ ($cm^2mol^{-1}s^{-1}$) and kinetic constant of half reaction k_o ($cm^2mol^{-1}s^{-1}$):

$$K_o(t) = k_o e^{\frac{\alpha_o n F}{RT} \cdot E(t)} \quad (13)$$

Hence the current density of the reaction $j_f(Am^{-2})$

$$j_f(t) = nF[R](0, t)K_o(t) \quad (14)$$

is only dependent of the applied voltage and the transport flow of the reducing species at the interface. The Faradaic impedance $Z_f = \Delta E / \Delta j_f$ (Ωcm^2) can be calculated by a first-order Taylor series expansion of the current density j_f (14):

$$\Delta j_f = \frac{\partial j_f}{\partial E} \Delta E + \frac{\partial j_f}{\partial [R](0)} \Delta [R](0) \quad (15)$$

With:

$$\frac{\partial j_f}{\partial [R](0)} = nFk_o e^{\alpha_o n E} = nFK_o \quad (16)$$

And

$$\frac{\partial E}{\partial j_f} = R_{ct} \quad (17)$$

Therefore the transformation in the Laplace plane of the equations (15) can be written:

$$Z_f(p) = R_{ct} - R_{ct}K_o \frac{\Delta [R](0, p)}{\Delta j_f(p)} \quad (18)$$

The current density and the flow of species transport are bound by the relation:

$$\Delta j_f(p) = -nF \Delta J_r(0, p) \quad (19)$$

Under the Nernst hypothesis seen in 3.2, the concentration profile is not disturbed beyond the characteristic length δ_r such as $\Delta [R](\delta_r, t) = 0$, and given boundary conditions at the interface $\Delta J_r(0, t) = -D_r \partial \Delta [R](x, t) / \partial x|_{x=0}$ ($molcm^{-2}s^{-1}$), the resolution in the Laplace plane of equation (8) gives the expression of the flow of species transport [20,21]:

$$\Delta J_r(0, p) = \Delta [R](0, p) \frac{D_r}{\delta_r^2} \left(\frac{\delta_r}{D_r p} \right)^{1/2} \coth \left(\frac{\delta_r}{D_r p} \right)^{1/2} \quad (20)$$

Therefore, equation (19) can directly be expressed as:

$$\frac{\Delta [R](0, p)}{\Delta j_f(p)} = \frac{1}{nF} \frac{\delta_r}{D_r} \frac{th \left(\frac{\delta_r}{D_r p} \right)^{1/2}}{\left(\frac{\delta_r}{D_r p} \right)^{1/2}} \quad (21)$$

And by defining:

$$R_\delta = \frac{R_{ct}K_o \delta_r}{D_r} \quad \text{and} \quad \tau_\delta = \frac{\delta_r^2}{D_r} \quad (22)$$

Eq. (18) can be written as the sum of a resistance and a Warburg diffusive element:

$$Z_f(p) = R_{ct} + W_\delta(p) \quad (23)$$

With:

$$W_\delta(p) = R_\delta \frac{th(\tau_\delta p)^{1/2}}{(\tau_\delta p)^{1/2}} \quad (24)$$

3.5. Faradaic impedance of a 2-step redox reaction with adsorbate

As mentioned in the introduction, zinc electrodeposition usually involves adsorbed species. The reference reaction involving adsorbed species is the Volmer - Heyrovsky one, which initially explained the H_2 evolution reaction but which has since been applied to many other cases as cation reduction [22,23].

This work proposes a new model involving two elementary steps but with a divalent cation, which is different although similar:



Therefore:

$$v_{r1}(t) = K_{r1}(t)[A^{2+}]^* \Gamma \theta_s(t) \quad (27)$$

$$v_{r2}(t) = K_{r2}(t) \Gamma \theta_{Ads}(t) \quad (28)$$

With:

$$K_{r1}(t) = k_{r1} e^{\frac{-\alpha_{r1} n F}{RT} \cdot E(t)} \quad (29)$$

$$j_f(t) = -F \Gamma (K_{r1}(t)[A^{2+}]^* \theta_s(t) + K_{r2}(t) \theta_{Ads}(t)) \quad (30)$$

$$\frac{d\theta_{Ads}}{dt} = K_{r1}[A^{2+}]^* \Gamma \theta_s(t) - K_{r2} \Gamma \theta_{Ads}(t) \quad (31)$$

$$\frac{d\theta_s}{dt} = K_{r2} \Gamma \theta_{Ads}(t) - K_{r1}[A^{2+}]^* \Gamma \theta_s(t) \quad (32)$$

$$\theta_s(t) + \theta_{Ads}(t) = 1 \quad (33)$$

The Faradaic impedance $Z_f = \Delta E / \Delta j_f$ can be calculated by a first-order Taylor series expansion of the current density j_f (30). The expression of the current density is explicitly a function of the electrode potential E, the coverage fraction of free sites θ_s , and of the adsorbed species θ_{Ads} .

$$\Delta j_f = \frac{\partial j_f}{\partial E} \Delta E + \frac{\partial j_f}{\partial \theta_s} \Delta \theta_s + \frac{\partial j_f}{\partial \theta_{Ads}} \Delta \theta_{Ads} \quad (34)$$

The system (30), (33) and (31) can be reformulated in the Laplace domain:

$$Z_f(p) = R_{ct} + R_{ct} F \Gamma K_{r1} [A^{2+}]^* \frac{\Delta \theta_s(p)}{\Delta j_f(p)} + R_{ct} F \Gamma K_{r2} \frac{\Delta \theta_{Ads}(p)}{\Delta j_f(p)} \quad (35)$$

$$p \Delta \theta_{Ads}(p) = (-\alpha_{r1} \Gamma K_{r1} [A^{2+}]^* \theta_s + \alpha_{r2} \Gamma K_{r2}) \Delta E(p) + K_{r1} [A^{2+}]^* \Delta \theta_s(p) - K_{r2} \Delta \theta_{Ads}(p) \quad (36)$$

$$\Delta \theta_s(p) + \Delta \theta_{Ads}(p) = 0 \quad (37)$$

The system (35), (36) and (37) can be solved using Sympy [24]. Introducing the total adsorbate impedance Z_θ , it can be written as a first order system:

$$\begin{aligned} Z_\theta(p) &= R_{ct} F \Gamma K_{r1} [A^{2+}]^* \frac{\Delta \theta_s(p)}{\Delta j_f(p)} + R_{ct} F \Gamma K_{r2} \frac{\Delta \theta_{Ads}(p)}{\Delta j_f(p)} \\ &= \frac{R_\theta}{1 + \tau_\theta p} \end{aligned} \quad (38)$$

The expression of R_θ and τ_θ follow:

$$R_\theta = \frac{R_{ct}(\alpha_{r1} - \alpha_{r2})(K_{r1}[A^{2+}]^* - K_{r2})}{2(\alpha_{r2} K_{r1}[A^{2+}]^* + \alpha_{r1} K_{r2})} \quad (39)$$

$$\tau_0 = \frac{(\alpha_{r1} + \alpha_{r2})}{2(\alpha_{r2}K_{r1}[A^{2+}]^* + \alpha_{r1}K_{r2})} \quad (40)$$

In this context, the impedance of this 2-step redox reaction with adsorbate can be modelled by an electrical RC circuit and can be capacitive or inductive. In the capacitive case, the parameters R, C are positive and negative in the inductive case.

4. Results

In order to interpret the experimental results, the expected main redox reactions involved in the zinc electrodeposition phase of the Ergosup process eq. (1) are:

At the cathode



At the anode



4.1. Polarization curves

The polarization curves in Fig. 6. I show the large variation of the $U(j)$ curves during the batch process. The $U(j)$ curves cross in two areas: about 450 Am^{-2} for the blue-orange and orange-green, and about 1630 Am^{-2} for the green-red and red-violet curves, revealing the presence of several physico-chemical phenomena. The uncorrected curves depicted in Fig. 6. I show that at high current densities the cell voltage is largely decreasing with deposition time, especially from current densities higher than 1000 Am^{-2} , whereas the cell voltage is almost constant at lower current densities. The appearance of the almost straight curves seems to indicate the preponderance of the ohmic drop over the electrode overvoltage, illustrating that at high current densities the ohmic resistance is the main contributing and varying effect of the steady state operating point. Indeed, according to eq. (5), conductivity increases considerably during the deposition step as concentrations change, approximately rising from 291 m Scm^{-1} to 823 m Scm^{-1} at 40°C . This increase of the conductivity results to a large decrease of R_Ω according to part 3.1.

The curves corrected from the ohmic drop are monotonically increasing with deposition time in Fig. 6. II, which means that the polarization resistance R_p is also monotonically increasing.

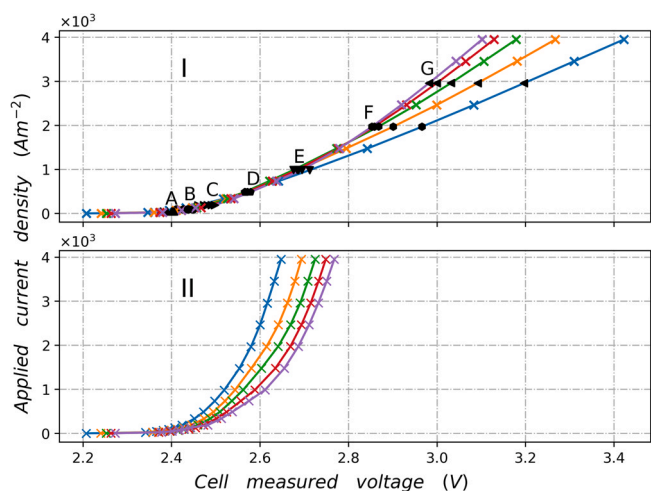


Fig. 6. Polarization curves without (I) and with (II) ohmic correction at deposit time (a) 3 min-blue, (b) 22.5 min-orange, (c) 45 min-green, (d) 67.5 min-red and (e) 90 min-purple. A, B, C, D, E, F, G correspond to the points studied by impedance spectroscopy.

$$R_p = \frac{dU_{cell}}{dj} - R_\Omega \quad (44)$$

The exponential shape of the curves seems to indicate the preponderance of charge transfer phenomena in the mixed reaction. At the anode, due to the abundance of water in the reaction medium its concentration is supposed to be almost constant, as it is for the surface area, the reaction kinetics, the temperature and the applied potential. Therefore a large variation of the anodic charge transfer resistance is not expected. On the contrary, the gradual depletion of Zn^{2+} ions is expected to influence the cathodic charge transfer resistance.

4.2. Impedance spectra

The seven impedance characterisations during the batch process in Fig. 7 show four distinct signatures in the Nyquist plane. In the order of descending frequencies, three capacitive loops are followed by an inductive loop at lower frequencies. The first two frequency capacitive signatures appear at the lowest current densities and regardless of the characterisation time. At 3000 Am^{-2} , plot G, the first one is almost no longer discernible and is only distinguished by its distance between the projection on the real axis of the highest frequency point and the effective cut-off of the abscissa axis. Graph D, at 500 Am^{-2} , the low frequency drift becomes chaotic, reflecting the appearance of another phenomenon. This new signature is also present in graph E before becoming a clear semicircle shape from 2000 Am^{-2} . The time evolution of the curves finally shows a last signature from 1000 Am^{-2} with the appearance of an inductive loop. The higher the current density, the faster this phenomenon occurs in the batch process: after 67.5 min at 1000 Am^{-2} , then 45 min at 2000 Am^{-2} and finally 22.5 min at 3000 Am^{-2} .

Fig. 8 compares the evolution of the polarization resistances during the batch process. Firstly, there is a trend of increasing resistance associated with the first two signatures. The 86 Hz frequency point is stable over time and indicates a minor variation in the capacitance associated with the second signature. Similarly, the 4 Hz frequency point changes very slightly and shows a relative decoupling of the high frequency phenomena on the left and the low frequency phenomena on the right. Therefore, the progressive appearance of the inductive loop is a reflection of the increase of the capacitance's value associated with the lowest frequencies.

Fig. 9 shows the characterisation at $t = 3$ min of deposit as a function of current density. This clearly demonstrates the decay of the resistances associated with the first two signatures with increasing current density. This is characteristic of charge transfer, whose resistance decay is inversely proportional to the current density in the case of Tafel's law. Indeed, the cell voltage of a Tafel reaction of type $Red \rightarrow Ox + ne^-$ is:

$$U_{cell} = U_{th} + \frac{RT}{\alpha nF} \ln\left(\frac{j}{j_0}\right) \quad (45)$$

And therefore the resistance dU_{cell}/dj is proportional to inverse of the current density.

Fig. 10 shows that, contrary to the signatures of the activation phenomena, the resistance associated with the last capacitive loop increases with the current density. The order of magnitude of this trend is more modest but becomes proportionally more important in the polarization resistance as j grows. This increase in a component of the polarization resistance as the current density and the associated electrode potential increase is characteristic of a mass transport phenomenon at the reaction layer.

Fig. 11, centred at the 4 Hz point, shows that the latter capacitive loop is only slightly sensitive to changes over time, and thus concentrations. However, in the case of two capacitive and inductive phenomena evolving simultaneously, the resultant of the two evolutions may hide wider variations of each phenomenon taken separately, and the interpretation of the low frequencies must be done with caution. The 4 Hz–50 mHz zoom at 3000 Am^{-2} does indeed show a greater variation and the presence of these

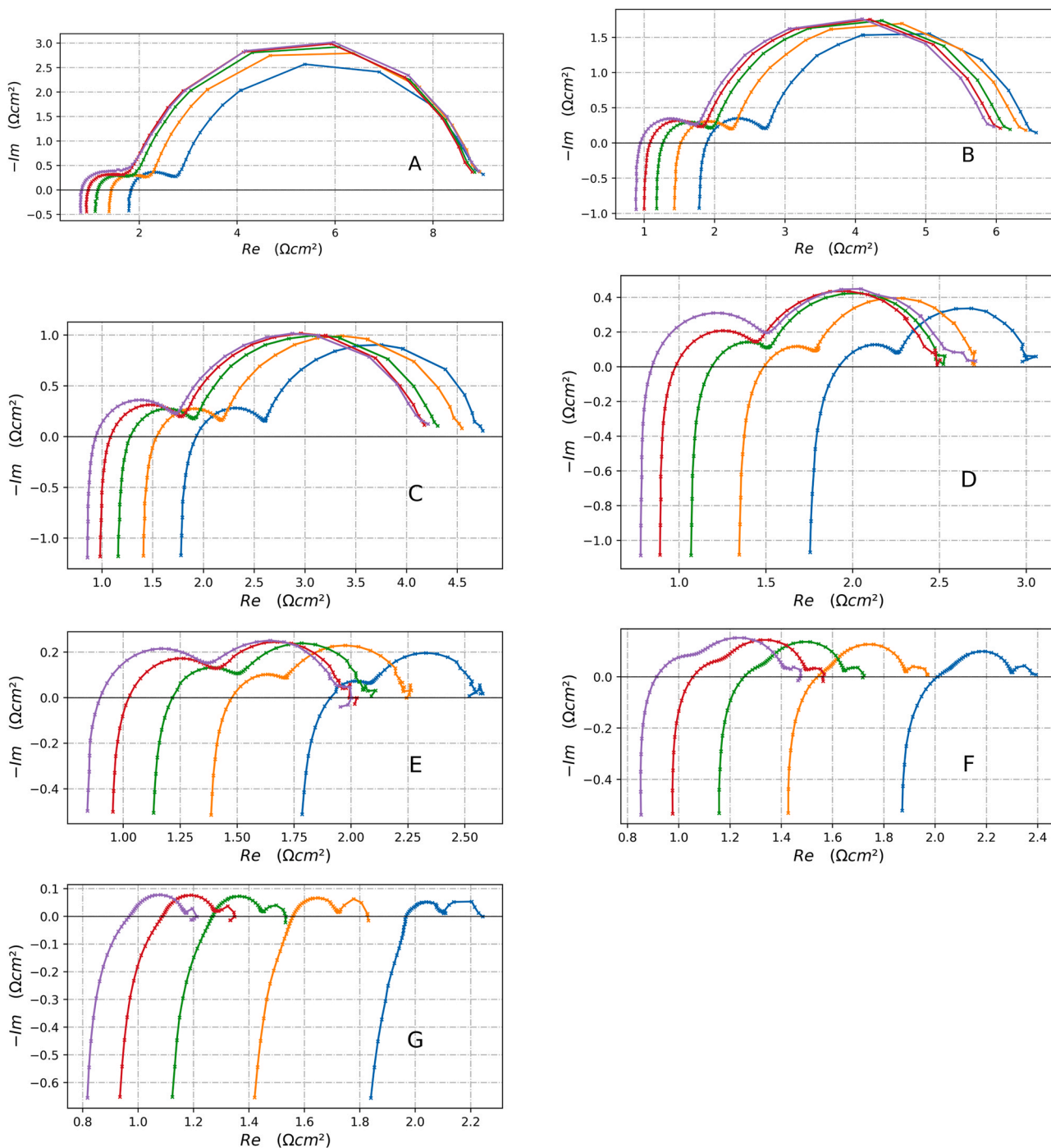


Fig. 7. Nyquist plots at deposit time (a) 3 min-blue, (b) 22.5 min-orange, (c) 45 min-green, (d) 67.5 min-red, (e) 90 min-purple and multiple current densities (A) 50 Am^{-2} , (B) 100 Am^{-2} , (C) 200 Am^{-2} , (D) 500 Am^{-2} , (E) 1000 Am^{-2} , (F) 2000 Am^{-2} and (G) 3000 Am^{-2} .

phenomena intermixed throughout the reaction, and illustrates the decrease of the associated resistive values.

Finally, Fig. 8 does not show a high-frequency signature that could reflect the evolution of hydrogen, suggesting that the charge transfer resistance is low compared to that of the zinc electrolysis.

5. Discussion

5.1. Modelling the impedance

Considering the interpretation of the presumed reaction mechanisms and the resulting Nyquist plots, we can propose a simplified

reaction mechanism for zinc electrodeposition that involves only a single adsorbed species, Zn_{ads}^+ . The model then follows the impedance model developed in section 2 for the reduction of a divalent cation and follows equations:



Given the assumption that the last capacitive loop is decreasing with time, a concentration impedance due to the water supply at the reaction site can be attributed to the OER, as modelled in section 3.4. Indeed, a lack of reagent supply to the cathode would have led to an increase in diffusive resistance R_{δ} over time. Supplementary experiments (refer to

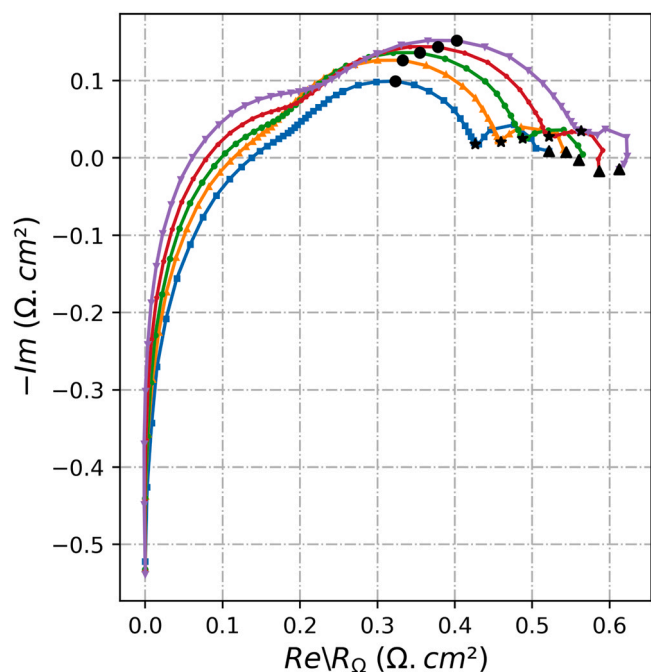


Fig. 8. Nyquist plots at 2000 Am^{-2} with ohmic drop correction at deposit time (a) 3 min-blue, (b) 22.5 min-orange, (c) 45 min-green, (d) 67.5 min-red and (e) 90 min-purple. • 86 Hz, ★ 4 Hz, ▲ 50 mHz.

Supplementary Materials) proved that this phenomenon is actually anodic. Other phenomena may explain the decrease in this resistance, such as the increase in hydrogen released which has the effect of homogenising the solution [25], or the bubble flow regime. This study does not allow to decide. Such an impedance has been seen studied in the case of alkaline electrolysis of water [26], which highlighted the importance of bubble size and production flow on impedance. The modelling of gas evolution by a Warburg diffusive element has also been reported in the case of reduction of CO_2 [27].

Thus, summarising the previous assumptions and adding the inductive effect L_{Ω} of the cell connection and the resistance of the electrolyte R_{Ω} , the general impedance of the system described in section 3 can be represented according to the electrical diagram shown in Fig. 12. Under ideal conditions where all time constants are sufficiently different that their frequency expressions are dissociated, the Nyquist plot of the ECM Fig. 12 is shown in Fig. 13. The various phenomena analysed are attributed to signatures in the Nyquist plane.

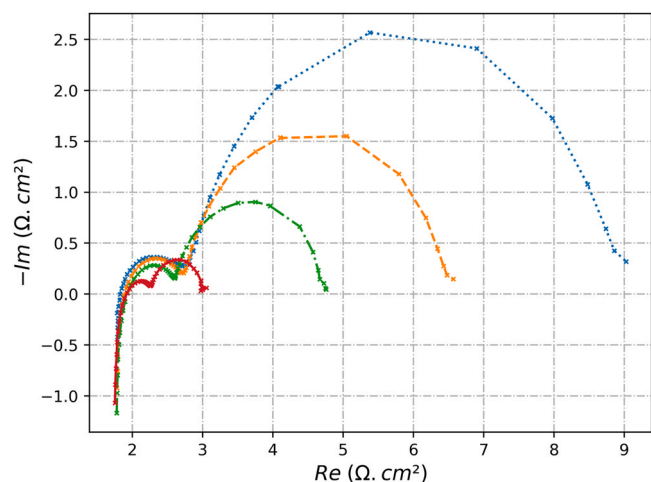


Fig. 9. Nyquist plots at 3 min deposit time (a) 50 Am^{-2} -blue, (b) 100 Am^{-2} -orange, (c) 200 Am^{-2} -green, (d) 500 Am^{-2} -red.

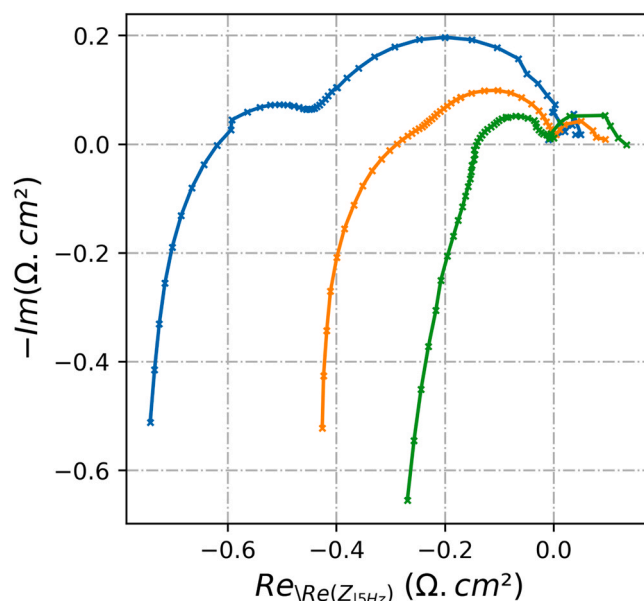


Fig. 10. Nyquist $\text{Re}(Z_{f=5\text{Hz}})$ centred plots at 3 min deposit time (a) 1000 Am^{-2} -blue, (b) 2000 Am^{-2} -orange, (c) 3000 Am^{-2} -green.

$$Z(j\omega) = L_{\Omega}j\omega + \frac{R_{ct1} + R_{\theta} + j\omega\tau_{\theta}}{(1 - \omega^2 R_{ct1} C_{dl1} \tau_{\theta}) + j\omega(R_{ct1} C_{dl1} + R_{\theta} + C_{dl1} \tau_{\theta})} + R_{\Omega} + \frac{R_{ct2} + W_s(j\omega)}{1 + j\omega C_{dl2}(R_{ct2} + W_s(j\omega))} \quad (48)$$

5.2. Simulating the impedance

To confirm the relevance of the model, it was simulated to reproduce the experimental curves at high current density. The parametrisation of the equivalent electrical model was performed with the python pymoo package [28] using the genetic algorithm UNSGA3. Thus, the data of the five EIS are included in the same objective

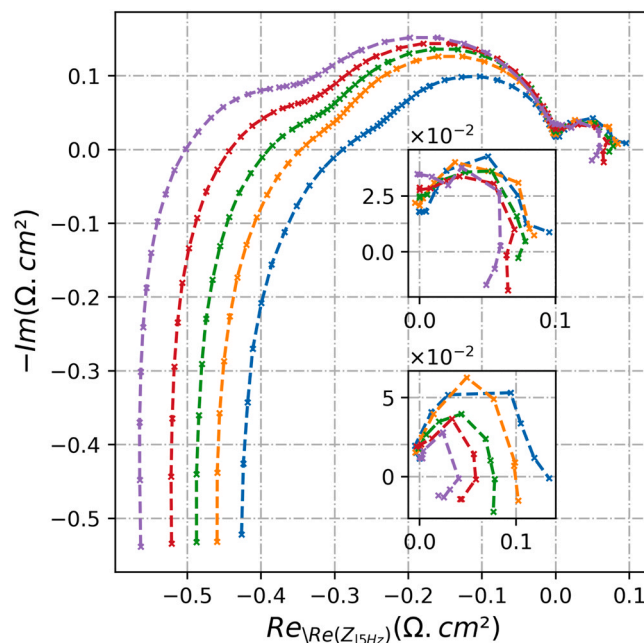


Fig. 11. Nyquist $\text{Re}(Z_{f=5\text{Hz}})$ centred plots at $j = 2000 \text{ Am}^{-2}$ and deposit time (a) 3 min-blue, (b) 22.5 min-orange, (c) 45 min-green, (d) 67.5 min-red, (e) 90 min-purple. Upper inset: Zoom for $j_{\text{EIS}} = 2000 \text{ Am}^{-2}$. Lower inset: Zoom for $j_{\text{EIS}} = 3000 \text{ Am}^{-2}$.

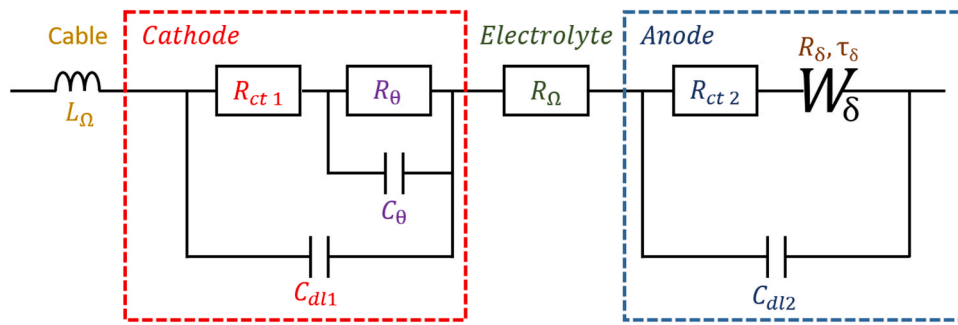


Fig. 12. Electrical equivalent circuit of the overall cell of zinc electrodeposition and corresponding impedance equation.

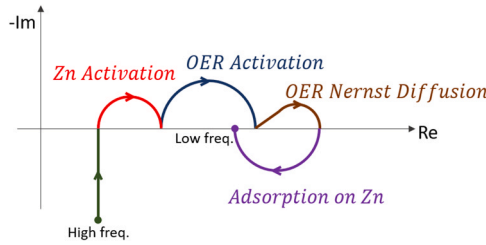


Fig. 13. Theoretical Nyquist plot with dissociated time constants.

function for minimising the deviation between measurement and modelling:

$$f_{obj} = \min \left(\sum_{EIS} \sum_f ((Re(Z_{Mod}) - Re(Z))^2 + (Im(Z_{Mod}) - Im(Z))^2) \right) \quad (49)$$

Some constraints are added to the optimizer, according to the analysis of the polarization and impedance curves in section 4:

- the parameter R_Ω is decreasing.
- the parameter C_θ is increasing.
- $R_{ct,1}C_{ct,1} < R_{ct,2}C_{ct,2}$.
- $R_{ct,2}C_{ct,2} < R_\theta C_\theta$.
- the resistance R_p is increasing.
- the imaginary part of R_p is positive.

The polarization resistance is defined as the impedance at 10^{-5} Hz, more than 100x lower than the minimum measurement frequency, and is chosen to be positive to indicate that the low frequency inductive loop is the last signature taken into account.

The impedance theorised by the previously developed equivalent electrical model has been optimised for the corrected impedance curves. As the model is visually globally overlapping the measurements,

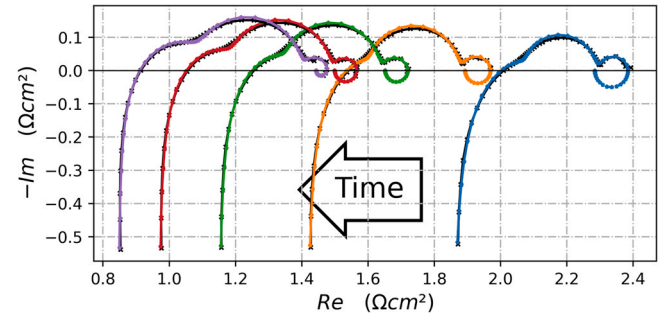


Fig. 14. Simulated impedance diagrams 2000 Am^{-2} and down to 1 mHz with Table 2 parameters at a) 3 min-blue, (b) 22.5 min-orange, (c) 45 min-green, (d) 67.5 min-red, (e) 90 min-purple. Black - Experimental measurements corresponding to 7.F.

the correlation coefficient R^2 is used to measure the correspondence between data and model. The impedance of the ECM Fig. 12 calculated with the parameters of Table 2 is shown in Fig. 14.

The modelled value R_Ω of Table 2 has an average deviation of 0.7% from the measured value and is systematically lower. This result is logical since the high frequency vertical asymptote is not reached during the measurement. Between the instants $t = 3 \text{ min}$ and $t = 90 \text{ min}$, the variation of total resistance evaluated at 2000 Am^{-2} is 16 % lower than the change of R_Ω , due to the increase in R_p compensating for the change of R_Ω . Therefore, the impedance spectra are over-corrected. Although imperfect, this result confirms the relevance of having corrected the deviation of the spectra on the Nyquist figure. A future study could focus on the temporal correction of the impedance curves by successive iterations of parametrizations and correction of the experimental data.

The number of parameters makes it difficult to compare with the literature. However, the value of the double layers can be discussed. The double-layer capacity of the cathode is of the usual order of magnitude of 10^{-4} Fcm^{-2} [9]. The double-layer capacity of the anode is

Table 2

Fitting parameters of the equivalent circuit model.

Parameters	3 min	22.5 min	45 min	67.5 min	90 min
L_Ω	$4.56 \cdot 10^{-6}$	$4.52 \cdot 10^{-6}$	$4.50 \cdot 10^{-6}$	$4.49 \cdot 10^{-6}$	$4.49 \cdot 10^{-6}$
R_Ω	$1.85 \cdot 10^{+0}$	$1.42 \cdot 10^{+0}$	$1.15 \cdot 10^{+0}$	$9.69 \cdot 10^{-1}$	$8.46 \cdot 10^{-1}$
$R_{ct,1}$	$2.18 \cdot 10^{-1}$	$1.88 \cdot 10^{-1}$	$2.00 \cdot 10^{-1}$	$2.18 \cdot 10^{-1}$	$2.41 \cdot 10^{-1}$
$C_{dl,1}$	$1.35 \cdot 10^{-4}$	$1.85 \cdot 10^{-4}$	$2.08 \cdot 10^{-4}$	$2.33 \cdot 10^{-4}$	$2.69 \cdot 10^{-4}$
$R_{ct,2}$	$2.10 \cdot 10^{-1}$	$2.65 \cdot 10^{-1}$	$2.81 \cdot 10^{-1}$	$2.95 \cdot 10^{-1}$	$3.06 \cdot 10^{-1}$
$C_{dl,2}$	$6.85 \cdot 10^{-3}$	$5.48 \cdot 10^{-3}$	$5.25 \cdot 10^{-3}$	$5.17 \cdot 10^{-3}$	$5.20 \cdot 10^{-3}$
R_δ	$1.03 \cdot 10^{-1}$	$1.01 \cdot 10^{-1}$	$9.24 \cdot 10^{-2}$	$8.89 \cdot 10^{-2}$	$8.88 \cdot 10^{-2}$
τ_δ	$1.11 \cdot 10^{+0}$	$9.47 \cdot 10^{-1}$	$7.38 \cdot 10^{-1}$	$6.26 \cdot 10^{-1}$	$4.22 \cdot 10^{-1}$
R_θ	$-1.02 \cdot 10^{-1}$	$-7.79 \cdot 10^{-2}$	$-7.08 \cdot 10^{-2}$	$-7.08 \cdot 10^{-2}$	$-3.76 \cdot 10^{-2}$
C_θ	$-4.40 \cdot 10^{+2}$	$-5.64 \cdot 10^{+2}$	$-2.46 \cdot 10^{+2}$	$-1.22 \cdot 10^{+2}$	$-9.80 \cdot 10^{+1}$
$dE/dj (\Omega\text{cm}^2)$	2.284	1.893	1.651	1.499	1.443
$R_p (\Omega\text{cm}^2)$	0.429	0.477	0.503	0.530	0.597
R^2	0.9990	0.9994	0.9995	0.9995	0.9995

also usual, authors have reported a similar value on Pb-Ag anodes [29] or on MMO anodes of different compositions [30,31].

The anodic and cathodic parameters are strongly consistent with each other when characterising the batch process (refer to [Supplementary Materials](#)). It is worth noting that the resistances associated with the signatures of the charge transfer phenomena are both globally increasing, and this is especially true for the OER. Moreover, the parameters associated with the adsorbate and diffusion phenomena are decreasing, although opposite in their expression on the Nyquist plane. As the diffusion resistance is more important, the resultant of these two phenomena tends to increase the resistance of the system. Thus, both phenomena contribute to the increase in polarization resistance as constrained in the algorithm. This parametrised model allows to represent the evolution of the polarization resistance during the batch process as observed on the polarization curves [Fig. 6](#).

6. Conclusion

In this study, the evolution of the polarization resistance of a zinc electrodeposition batch process at high current density during 90 min was investigated by means of impedance spectroscopy and polarization curves. The batch process starts with a high concentration of zinc and is subject to a very wide variation not recorded in the literature. At both electrodes, simplified reaction mechanisms are used. This assumption has led to the development of an equivalent electrical model, as shown in [Fig. 12](#), which accounts for the various phenomena observed during the process. The predominant physical phenomena at high current densities can be summarised as follows:

1. The zinc electrodeposition mechanism can be modelled by a two steps mechanism, showing charge transfer and adsorption phenomena.
2. Hydrogen evolution does not appear to leave a signature.
3. The oxygen evolution reaction can be modelled by an electrochemical step showing charge transfer and diffusive phenomena.

The model is able to reproduce the experimental impedance curves at high current densities with high correlation coefficients ($R^2 > 0.9990$). The fitting parameters used in the model are consistent with the literature and the observations made, showing an increase in the polarization resistance throughout the batch process. The equivalent circuit model, with its parameters, can provide useful insights into the behavior of zinc electrodeposition systems.

Nevertheless, there are still some aspects that could be improved. The temporal correction of impedance curves by successive iterations of parametrizations and correction of experimental data may lead to more accurate results. Furthermore, the non-uniform charge distribution on the anode surface could lead to the use of a constant phase element (CPE), which would increase both the accuracy of the model but also the complexity of the optimization algorithm.

Overall, this study has provided a comprehensive analysis of the impedance behavior of zinc electrodeposition systems during a batch process. The proposed model, with its fitting parameters, has proven to be a valuable tool in understanding and predicting the evolution of impedance in such systems. This work was developed with the aim of establishing the diagnosis of an electrolysis cell with a perspective of studying on the ageing of this process, as well as studying direct coupling with renewable energy sources. This work may serve as a foundation for further research in this area, ultimately contributing to the optimization and development of more efficient zinc electrodeposition processes.

Declaration of Competing Interest

The authors declare the following financial interests/personal relationships which may be considered as potential competing interests:

Leo FAYARD reports financial support was provided by Ergosup. Leo FAYARD reports a relationship with Ergosup that includes: employment. Co-authors Vincent FEYNEROL and Vincent BIZOUARD are employees of Ergosup.

Acknowledgement

This research was supported by Ergosup which provided funding. The funding agency played no role in the design, execution, or interpretation of the study. The authors would like to express their gratitude to Ergosup for their support.

Appendix A. Supporting information

Supplementary data associated with this article can be found in the online version at [doi:10.1016/j.ijoes.2023.100185](https://doi.org/10.1016/j.ijoes.2023.100185).

References

- [1] IEA, Global hydrogen review 2022, 70, Paris, License: CC BY 4.0. <https://www.iea.org/reports/global-hydrogen-review-2022>.
- [2] Ergosup. <https://www.ergosup.com/> 2023.
- [3] A.C. Scott, R.M. Pitblado, G.W. Barton, A.R. Ault, Experimental determination of the factors affecting zinc electrowinning efficiency, *J. Appl. Electrochem.* 18 (1988), <https://doi.org/10.1007/BF01016215> (Jan.).
- [4] M.J. Mahon, Dynamic Process Simulation of Zinc Electrowinning, University of British Columbia, 2016, <https://doi.org/10.14288/1.0223280> Ph.D. thesis.
- [5] A.M. Alfantazi, D.B. Dreisinger, The role of zinc and sulfuric acid concentrations on zinc electrowinning from industrial sulfate based electrolyte, *J. Appl. Electrochem.* 31 (6) (2021) 641–646.
- [6] I. Epelboin, M. Ksouri, R. Wiart, On a model for the electrocrystallization of zinc involving an autocatalytic step, *J. Electrochem. Soc.* 122 (9) (1975) 1206–1214, <https://doi.org/10.1149/1.2134426>
- [7] R. Ichino, C. Cachet, R. Wiart, Mechanism of zinc electrodeposition in acidic sulfate electrolytes containing Pb²⁺ ions, *Electrochim. Acta* 41 (7) (1996) 1031–1039, [https://doi.org/10.1016/0013-4686\(95\)00435-1](https://doi.org/10.1016/0013-4686(95)00435-1)
- [8] C. Cachet, R. Wiart, Zinc electrowinning in acidic sulfate electrolytes: impedance analysis and modeling of the influence on nickel impurities, *J. Electrochem. Soc.* 141 (1) (1994) 131–140, <https://doi.org/10.1149/1.2054672>
- [9] C. Cachet, R. Wiart, Zinc deposition and passivated hydrogen evolution in highly acidic sulphate electrolytes: depassivation by nickel impurities, *J. Appl. Electrochem.* 20 (6) (1990) 1009–1014, <https://doi.org/10.1007/BF01019581>
- [10] C. Cachet, R. Wiart, J. Zoppas-Ferreira, Zinc deposition and dissolution in a flow-through porous electrode, *Electrochim. Acta* 38 (2–3) (1993) 311–318, [https://doi.org/10.1016/0013-4686\(93\)85145-0](https://doi.org/10.1016/0013-4686(93)85145-0)
- [11] I. Epelboin, M. Ksouri, R. Wiart, Kinetics of zinc electrocrystallization correlated with the deposit morphology, *Faraday Symp. Chem. Soc.* 12 (1977) 115–125, <https://doi.org/10.1039/FS9771200115>
- [12] C. Cachet, R. Wiart, Influence of a perfluorinated surfactant on the mechanism of zinc deposition in acidic electrolytes, *Electrochim. Acta* 44 (26) (1999) 4743–4751, [https://doi.org/10.1016/S0013-4686\(99\)00223-6](https://doi.org/10.1016/S0013-4686(99)00223-6)
- [13] E. Guerra, Evaluation of Zinc Electrodeposition Kinetics from Acidic Zinc Sulfate Solutions Using a Upd Modified Platinum Substrate, (Ph.D. thesis), University of British Columbia, 2003.
- [14] A. Lasia, *Electrochemical Impedance Spectroscopy and its Applications*, Springer, New York, NY, 2014, <https://doi.org/10.1007/978-1-4614-8933-7>
- [15] S.M. Nawale, M.M. Dlamini, F.-B. Weng, Analyses of the effects of electrolyte and electrode thickness on high temperature proton exchange membrane fuel cell (h-tpemfc) quality, *Membranes* 13 (1) (2023), <https://doi.org/10.3390/membranes13010012> <https://www.mdpi.com/2077-0375/13/1/12>.
- [16] K. Zhuo, C.Y. An, P.K. Kannan, N. Seo, Y.-S. Park, C.-H. Chung, Effect of electrolyte composition on the morphological structures of dendritic copper powders prepared by a spontaneous galvanic displacement reaction, *Korean J. Chem. Eng.* 34 (5) (2017) 1483–1489, <https://doi.org/10.1007/s11814-017-0023-3>
- [17] L. Sigrist, O. Dossenbach, N. Ibl, On the conductivity and void fraction of gas dispersions in electrolyte solutions, *J. Appl. Electrochem.* 10 (2) (1980) 223–228, <https://doi.org/10.1007/BF00726089>
- [18] H. Vogt, Mechanisms of mass transfer of dissolved gas from a gas-evolving electrode and their effect on mass transfer coefficient and concentration overpotential (Sep.), *J. Appl. Electrochem.* 19 (1989), <https://doi.org/10.1007/BF01320646> (Sep.).
- [19] E. Guerra, M. Bestetti, Physicochemical properties of ZnSO₄-H₂SO₄-H₂O electrolytes of relevance to zinc electrowinning, 2023.
- [20] J.-P. Diard, B. Le Gorrec, C. Montella, *Cinétique électrochimique*, HERMANN Éditions, 1996.
- [21] M.E. Orazem, B. Tribollet, *Electrochemical Impedance Spectroscopy. The Electrochemical Society Series*, Wiley, Hoboken, N.J., 2008 (oCLC: ocn144517368).
- [22] J.P. Diard, B.L. Gorrec, C. Montella, C. Montero-Ocampo, Second order electrochemical impedances and electrical resonance phenomenon, *Electrochim. Acta* 37 (1) (1992) 177–179, [https://doi.org/10.1016/0013-4686\(92\)80027-J](https://doi.org/10.1016/0013-4686(92)80027-J)

- [23] V. Kichigin, A. Shein, Influence of hydrogen absorption on the potential dependence of the Faradaic impedance parameters of hydrogen evolution reaction, *Electrochim. Acta* 201 (2016) 233–239, <https://doi.org/10.1016/j.electacta.2016.03.194>
- [24] A. Meurer, C.P. Smith, M. Paprocki, O. Čertík, S.B. Kirpichev, M. Rocklin, A. Kumar, S. Ivanov, J.K. Moore, S. Singh, T. Rathnayake, S. Vig, B.E. Granger, R.P. Muller, F. Bonazzi, H. Gupta, S. Vats, F. Johansson, F. Pedregosa, M.J. Curry, A.R. Terrel, V. Roučka, A. Saboo, I. Fernando, S. Kulal, R. Cimrman, A. Scopatz, Sympy: symbolic computing in python, *PeerJ Comput. Sci.* 3 (2017) e103, <https://doi.org/10.7717/peerj-cs.103>
- [25] L. Janssen, J. Hoogland, The effect of electrolytically evolved gas bubbles on the thickness of the diffusion layer—II, *Electrochim. Acta* 18 (8) (1973) 543–550, [https://doi.org/10.1016/0013-4686\(73\)85016-9](https://doi.org/10.1016/0013-4686(73)85016-9)
- [26] J. Schillings, *Etude numérique et expérimentale d'écoulements diphasiques: application aux écoulements à bulles générées par voie électrochimique*, Université Grenoble Alpes, 2017 Ph.D. thesis.
- [27] S. Lettieri, J. Zeng, M.A. Farkhondehfar, U. Savino, M. Fontana, C.F. Pirri, A. Sacco, Correlation between impedance spectroscopy and bubble-induced mass transport in the electrochemical reduction of carbon dioxide, *J. Energy Chem.* 67 (2022) 500–507, <https://doi.org/10.1016/j.jechem.2021.10.023>
- [28] J. Blank, K. Deb, *pymoo: Multi-objective optimization in python*, *IEEE Access* 8 (2020) 89497–89509.
- [29] C. Cachet, C. Rerolle, R. Wiart, Kinetics of Pb and Pb-Ag anodes for zinc electrowinning—II. Oxygen evolution at high polarization, *Electrochim. Acta* 41 (1) (1996) 83–90, [https://doi.org/10.1016/0013-4686\(95\)00281-1](https://doi.org/10.1016/0013-4686(95)00281-1)
- [30] H.M. Abbasi, K. Jafarzadeh, S.M. Mirali, An investigation of the effect of RuO₂ on the deactivation and corrosion mechanism of a Ti/IrO₂ + Ta₂O₅ coating in an OER application, *J. Electroanal. Chem.* 777 (2016) 67–74, <https://doi.org/10.1016/j.jelechem.2016.07.036>
- [31] R. Alibek, M. Atapour, A. Aghajani, R. Ashari, Microstructure and electrochemical properties of IrO₂ + RhOx + ZrO₂ coated titanium anodes, *Electrochim. Acta* 329 (2020) 135158, <https://doi.org/10.1016/j.electacta.2019.135158>